Evaluation of tungsten influx rate using line emissions from W^{5+} ions in EAST tokamak

Fengling Zhang[1,2] , **Darío Mitnik**[1,3,*] , **Ling Zhang**[1,*] , **Runjia Bao**[1,2],
Wenmin Zhang[1,2] , **Shigeru Morita**[1,4] , **Yunxin Cheng**[1] , **Ailan Hu**[1], **Chengxi Zhou**[1],
Jihui Chen[1], **Xiaobin Ding**[5] , **Yinxian Jie**[1] **and Haiqing Liu**[1]

[1] Institute of Plasma Physics, Hefei Institutes of Physical Science, Chinese Academy of Sciences, Hefei 230031, China
[2] University of Science and Technology of China, Hefei 230026, China
[3] Instituto de Astronomía y Física del Espacio (CONICET-Universidad de Buenos Aires), Buenos Aires 1428, Argentina
[4] National Institute for Fusion Science, Toki 509-5292, Gifu, Japan
[5] Key laboratory of Atomic and Molecular Physics & Functional Materials of Gansu Province, College of Physics and Electronic Engineering, Northwest Normal University, Lanzhou 730070, China

E-mail: dmitnik@df.uba.ar and zhangling@ipp.ac.cn

Abstract

The S/XB ratios (ionization events per emitted photon) allow one to relate spectroscopic emissivity measurements to the impurity influx from a localized source. In this work, we determine the tungsten influx by examining two dominant extreme ultraviolet line emissions at 382.13 Å and 394.07 Å, corresponding to the $4f^{14}5f \rightarrow 4f^{14}5d$ radiative transitions of the W^{5+} ion. The ground configuration of W^{5+} consists of the ground level and a metastable level, with the latter having a higher population than the ground state. Therefore, a simple approach assuming that the transitions are independent, i.e. only populated by a unique level source, requires correction. To address this, we have developed a fully collisional-radiative modeling in which 430 levels contribute to the ionization. We have utilized three advanced computational codes – HULLAC (Hebrew University—Lawrence Livermore Atomic Code, AS (AutoStructure), and FAC (Flexible Atomic Code) – for the atomic structure calculations. These codes provide the necessary information such as wavelengths, collisional and radiative transition rate coefficients. The FAC code was also used to calculate the direct electron-impact ionization under the distorted-wave approximation. We also included contributions to total ionization from excitation-autoionization processes up to $n = 15$ manifolds from the distorted-wave calculations. Subsequently, we used these results to ascertain the tungsten impurity influx in a dedicated discharge of the EAST tokamak, which operates with full tungsten divertors. In our findings, we observed that for the density range relevant to the edge region of a tokamak plasma, the S/XB ratios are almost independent of electron density but exhibit significant variation with electron temperature.

---

* Authors to whom any correspondence should be addressed.

1. Introduction

Various intrinsic impurities are inevitably generated in tokamak discharges due to the interaction between plasma and wall. Impurities ionized in the core release a large number of electrons, severely diluting the concentration of the primary plasma and affecting the reaction power density of fusion, decreasing the overall performance of the plasma. Therefore, monitoring and controlling the entry of impurities into the core are an important issue for long-pulse discharge operations.

It is possible to relate spectroscopic measurements of emissivities from an impurity ion to the impurity influx into the plasma core. Behringer *et al* [1] proposed the use of the 'ionization per emitted photon' S/XB ratio, also known as the 'inverse photon efficiency', denoting the number of ionization events per observed photons (incoming ions over emitted photons). The S/XB ratios have been used to evaluate the influx in tokamak devices of common light impurities such as carbon, nitrogen, oxygen, and neon, as well as metal impurities such as chromium, iron, nickel, molybdenum, and others [1–5].

Tungsten has been selected as the divertor and first wall material for ITER due to its high melting point, high thermal conductivity, low sputtering rate, low tritium retention rate, and low neutron activation rate [6]. However, highly ionized tungsten ions in the core and edge emit intense radiation at various wavelength ranges, which can cause significant radiation power loss and severely reduce plasma confinement performance. Therefore, evaluating the amount of tungsten entering through the edge is crucial for functioning high confinement long pulse plasma. Many extensive studies have been dedicated to the evaluation of the tungsten influx using the 4009 Å spectroscopic line of W I [7–9]. Other lines from W I have been used by Beigman *et al* [10], and W II was used by Pospieszczyk *et al* [11]. Ballance *et al* [12] conducted a detailed study on the S/XB ratios for the 1099.05 Å, 1119.7 Å, 1172.47 Å, and 1186.17 Å lines of W^{3+}, assuming these lines as independent. Dong *et al* [13] evaluated the influx rate of W^{6+} using the S/XB coefficients calculated with the ADAS code [14].

Recently, the spectrum of W^{5+} was observed during EAST discharge, which provides us with the necessary experimental spectrum for further studying the S/XB of low-ionized tungsten ions. As pointed out by Behringer *et al* [1], data for any particular ionization stage of the atomic species of interest can be employed as long as no higher ionization stages of that atom emerge from the localized source. Thus, such spectroscopic measurements for specific radiative transitions in W^{5+} would allow for the determination of the influx of tungsten.

The most straightforward approach for the S/XB determination is to assume that only one ground (or metastable) level populates the upper level of the observed spectral line. Even if the effects of collisions to and cascades from higher lying levels are considered, this simple approximation only works for some cases, as shown in the following sections. In general, we must take allowance that the source of the level population can also arise from other metastables and not only from a unique level, the so-called *metastable cross-coupling approach* [3].

The paper is organized as follows. In section 3, we develop the main formulas needed for the evaluation of the S/XB coefficients. First, we show in 3.1 details about how to employ the rate coefficients for excitations and radiative decays into a quasistatic generalized collisional-radiative level population model. With this, we obtain the effective contribution to the population of the excited states involved in the radiative transitions to study. In 3.2, we show how to use these coefficients to determine S/XB ratios as a function of electron density and temperature. We realized that many works deal with cases in which only the ground level is populated or cases in which the emissivity in the metastable line could be considered independent (namely, the upper levels are only populated by direct excitation from a unique source). However, the discussion for cross-coupled metastables, in which the populations of the upper levels arise from different sources, is scarce and worth developing in detail. In section 3.4, we briefly describe the three computational codes used in our calculations for the atomic structure. In section 4, we show the results, first for the atomic structure calculations in 4.1. Then, we present the results obtained for a model consisting of only four levels, which accounts for most of the relevant physical processes involved, at least within the density and temperature range of interest for Tokamak plasmas. Following that, we solve a full collisional-radiative model with 430 levels, and present and discuss the final S/XB coefficients. We conclude with some final remarks in section 5.

2. Experimental setup

EAST is a fully superconducting tokamak device equipped with ITER-like active water-cooled W/Cu monoblocks tungsten divertors, capable of high-power long pulse operation. The main parameters are: major radius $R \leqslant 1.9$ m, minor radius $a \leqslant 0.45$ m, plasma current $I_p \leqslant 1$ MA, and toroidal magnetic field $B_T \leqslant 3.5$ T [15–17]. Presently, various auxiliary heating and current driving have been installed, including two lower hybrid current drive (LHCD) systems, an electron cyclotron heating (ECH) system, an ion cyclotron resonant frequency (ICRF) system, and balanced neutral beam injection (NBI) systems [18]. A set of flat-field extreme ultraviolet (EUV) spectrometers, working in the 20–500 Å wavelength range with fast time response (5 ms/frame), named EUV_long [19], was developed to measure line emissions and to monitor

the impurities present in the EAST plasmas. A laminar-type varied-line-spacing concave holographic grating 1200 grooves mm^{-1} is fixed at grazing incidence 87° with a narrow entrance slit width of 30 μm for increasing the spectral resolution. A back-illuminated charge-coupled device (CCD) with a total size of 26.6 × 6.6 mm^2 and pixel numbers of 1024 × 255 (26 × 26 μm^2/pixel) is used for recording the spectrum. The wavelength calibration is performed by cubic polynomial fitting with many well-known spectral lines covering the observable range [20]. An absolute calibration, in which the raw measured spectral counts are converted into absolute spectral intensities, is further achieved by comparing the observed and calculated intensities of EUV and visible bremsstrahlung continua, a procedure explained in previous works [19–22].

Figure 1(left part) displays the operating parameters of EAST plasma discharge #100 300 as a function of time. The upper part (*a*) displays the plasma current I_p. Part (*b*) presents the electron temperature of the core plasma T_{e0} provided by the electron cyclotron emission (ECE) system [23] and the line-averaged electron density n_e measured by the hydrogen cyanide (HCN) interferometer system [24]. Part (*c*) depicts the heating power of ECRH, LHW, and NBI. Part (*d*) shows the total radiation power loss measured by the AXUV (absolute EUV) photodiode array [25]. Finally, part (*e*) presents the emission intensity of the two dominant W^{5+} EUV spectral lines at 382.13 Å and 394.07 Å, which are used here to determine the total flux of tungsten. These two lines are not frequently observed in general discharges. As the figure indicates,

they do not appear during the initial and flat-top stages of the discharge, likely due to a significant reduction in throughput at longer wavelengths in the current grazing-incidence EUV spectrometer. However, at $t \approx 5.2$ s, high-intensity W^{5+} lines are detected. This is attributed to strong plasma-wall interactions (PWIs) that ultimately lead to plasma termination. Therefore, we focus on the plasma behavior at this final stage of the discharge, during the time interval $t = 5.10 - 5.25$ s, as depicted in the right part of figure 1. As shown in part (*d*), the radiation power loss begins to increase at time $t = 5.14$ s due to core tungsten accumulation. This accumulation causes the plasma to cool down dramatically, as illustrated in part (*b*). When the electron temperature is relatively low, for instance, when $T_{e0} \leqslant 1.0$ keV, the emission volume of the W^{5+} lines increases, and meanwhile, the tungsten source increases mainly due to this strong PWI, then high-intensity spectral lines of W^{5+} at 382.13 Å and 394.07 Å could be observed, as shown in part (*e*).

Figure 2 displays the 280–440 Å spectral range for the EAST discharge #100 300 at two different times. The brown curve was obtained at time $t = 5.150$ s, when no trace of W was found in the plasma, and the black curve was obtained at time $t = 5.200$ s when the W intensity reached its maximum. Before the burst, only some lines emitted from HeII, Fe XVI, CIV, and CV are observable in this spectral range. The lines observed at the W peak intensity have been identified [26, 27] as belonging to different low-charged W ions, as indicated in the figure. The strong lines in the 280–320 Å range are associated with the $5p^6 \rightarrow 5p^5 5d$ transitions of W^{6+}, and from this

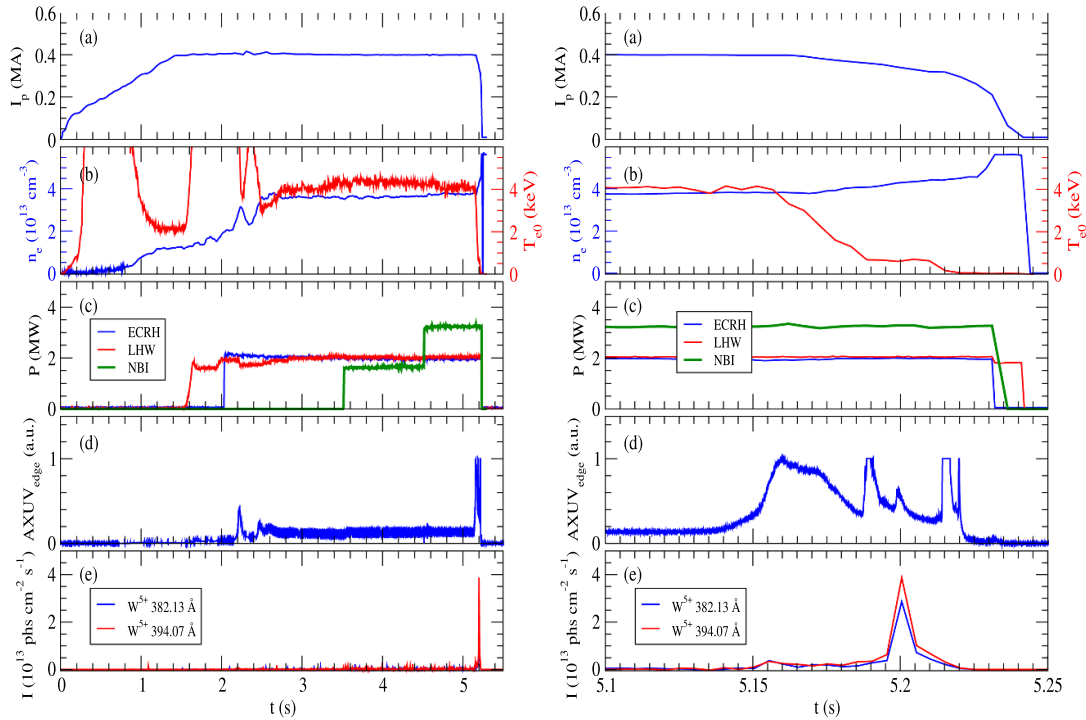**Figure 1.** Evolution of specific parameters for the EAST discharge #100 300. (*a*) Plasma current I_p. (*b*) Central electron temperature, T_{e0}, and line-averaged electron density, n_e. (*c*) Heating power of ECRH, LHW, and NBI. (*d*) Boundary radiation power loss. (*e*) W^{5+} emission line intensities at 382.13 Å (blue), and 394.07 Å (red). Right Part: Zoom at $t = 5.10 - 5.25$ s.
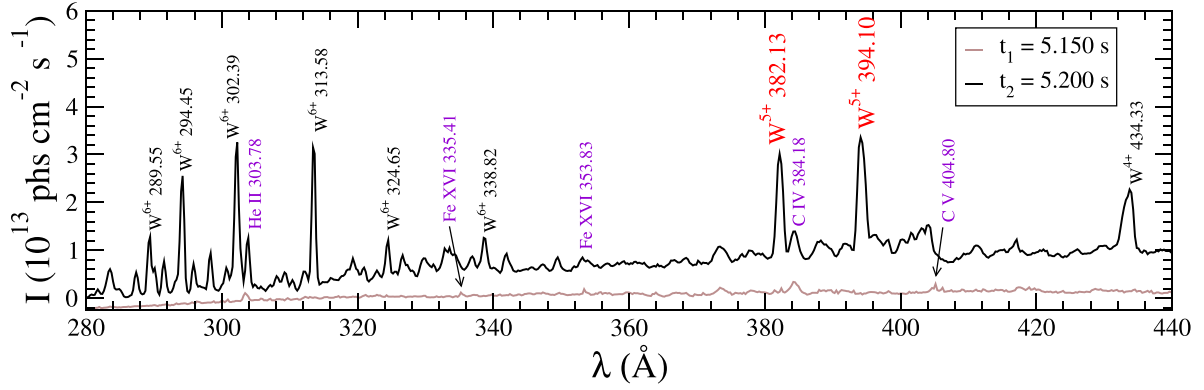
Figure 2. EAST spectra obtained at discharge #100 300 with the b_long spectrometer. Brown curve: observed at $t = 5.150$ s, before the W burst. Black curve: observed at $t = 5.200$ s, at the maximum of *W* intensity.

ion, the $4f^{13}5s^25p^65d \rightarrow 4f^{13}5s^25p^65f$ lines are also observed. The line at 434.33 Å, corresponds to the $5d^2 \rightarrow 5d7p$ transition of W^{4+}. In the region around 400 Å, two prominent lines are highlighted. We have identified these lines as corresponding to $5f \rightarrow 5d$ transitions of W^{5+}; the line at 382.13 Å is emitted by the $(4f^{14}5f)_{\frac{5}{2}} \rightarrow (4f^{14}5d)_{\frac{3}{2}}$ transition, and the line at 394.07 Å arises from the $(4f^{14}5f)_{\frac{7}{2}} \rightarrow (4f^{14}5d)_{\frac{5}{2}}$ transition. As we shall see later, these lines will provide the spectroscopic information necessary to determine the amount of tungsten flux entering the plasma.

3. Theoretical methods

3.1. Collisional radiative model

To determine the impurity influx for a particular element using the photon emission from a particular ion, one needs to know the population of the excited levels of this ion. To calculate the population n_j of the excited levels j of a particular impurity ion, we solve for a given electronic density and temperature, the collisional-radiative equations:

$$\frac{dn_j}{dt} = \sum_{k>j} n_k \left(A_{kj} + n_e Q_{kj}\right) + \sum_{i<j} n_i n_e Q_{ij}$$
$$- n_j \left(\sum_{i<j} \left(A_{ji} + n_e Q_{ji}\right) + \sum_{k>j} n_e Q_{jk}\right) =$$
$$= \sum_m C_{jm} n_m, \qquad (1)$$

where n_e is the electronic density, A_{ji} are the radiative rate coefficient for transitions from level j to level i. Q_{ji} are the electron-impact excitation rate coefficients if $i > j$, and the deexcitation rates if $i < j$. In matrix form, equation (1) is

$$\frac{d\vec{n}}{dt} = \mathbf{C} \cdot \vec{n} \qquad (2)$$

where the elements of the matrix $\mathbf{C}$ are

$$C_{jm} \equiv \begin{cases} A_{mj} + n_e Q_{mj} & \text{for } m > j \\ n_e Q_{mj} & \text{for } m < j \\ -\left(\sum_{i<j}(A_{ji} + n_e Q_{ji}) + \sum_{k>j} n_e Q_{jk}\right) & \text{for } m = j. \end{cases}$$
$$(3)$$

We partition the complete set of levels into metastables (denoted by greek letters $\sigma, \rho, \dots, \mu$), and excited levels (denoted here with roman letters $i, j, \dots, n$)

$$\vec{n} = \begin{pmatrix} \vec{n}_\tau \\ \vec{n}_s \end{pmatrix} \qquad (4)$$

and assume a quasi–static approximation in which the population of the excited levels are relaxed relative to the ground and metastable levels:

$$\frac{d\vec{n}_\tau}{dt} \neq 0 \qquad \text{and} \qquad \frac{d\vec{n}_s}{dt} = 0. \qquad (5)$$

Under this approximation, equation (2) becomes

$$\begin{pmatrix} \frac{d\vec{n}_\tau}{dt} \\ \hline \frac{d\vec{n}_s}{dt} = 0 \end{pmatrix} = \begin{pmatrix} & \Big| & \\ \hline \mathbf{C}_\tau & \Big| & \mathbf{C}_s \end{pmatrix} \begin{pmatrix} \vec{n}_\tau \\ \hline \vec{n}_s \end{pmatrix}. \qquad (6)$$

To solve this problem, we take only the excited-levels part of the matrix, having the following equation

$$0 = \mathbf{C}_\tau \cdot \vec{n}_\tau + \mathbf{C}_s \cdot \vec{n}_s \qquad (7)$$

The solution for the excited levels is

$$\vec{n}_s = [\mathbf{C}_s]^{-1} \cdot [-\mathbf{C}_\tau] \cdot \vec{n}_\tau \equiv n_e \mathcal{F} \cdot \vec{n}_\tau. \qquad (8)$$

The matrix $\mathcal{F}$ denotes the effective contribution to the population of the excited levels via excitations from the metastables.

This is the usual notation used in the field, in which $\mathcal{F}_{i\rho}$ represents the effective contribution to the population of i due to excitations from the metastable ρ.

3.2. S/XB—ionization events per photon

The neutral impurity particles entering the tokamak plasma from the wall are ionized in a narrow region around the surface. Neglecting recombination processes, the inward impurity influx density is equal to the ionization rate per unit surface area, integrated over the extension of the region towards the center of the plasma. Behringer *et al* have shown [1] that for the calculation of the inward flux, it is enough to choose an ionization degree Z of the impurity ions sufficiently small to ensure that no ions emerge from the sputtering surface in higher ionization stages. In that case, the inward flux along the line-of-sight ξ up to stage Z becomes the overall impurity flux, which is related to the integral over the abundances of the metastables of stage Z alone:

$$\Gamma = \Gamma_\sigma = \int_0^\infty n_e \sum_\sigma S_\sigma(\xi)\, n_\sigma(\xi)\, d\xi , \qquad (9)$$

where S_σ is the ionization rate coefficient from metastable level σ of the impurity ion of charge Z. Since a ionization event is followed by the emission of spectral lines, it is possible to relate the number of emitted photons with the flux. Considering the radiative transition from a level j to a lower level i and supposing that the upper-level j is populated only from levels excited from a unique metastable σ, the strength of a spectral line produced by the radiative transition $j \rightarrow i$ is proportional to its emissivity

$$\epsilon_{\sigma, i \rightarrow j} = A_{ij} n_i \qquad (10)$$

and the corresponding line-of-sight emissivity is defined by

$$I_{\sigma, i \rightarrow j} = \int_0^\infty \epsilon_{\sigma, i \rightarrow j}(\xi)\, d\xi . \qquad (11)$$

Substituting in the flux equation (9) and taking into account that for only one metastable

$$\mathcal{F}_{i\sigma} = \frac{1}{n_e} \frac{n_i}{n_\sigma} \qquad (12)$$

the flux becomes [1]:

$$\Gamma_\sigma = \int_0^\infty n_e S_\sigma(\xi)\, n_\sigma(\xi)\, d\xi \approx \frac{S_\sigma}{A_{ij} \mathcal{F}_{i\sigma}} \int_0^\infty A_{ij} n_i(\xi)\, d\xi =$$
$$= \frac{S_\sigma}{A_{ij} \mathcal{F}_{i\sigma}} I_{\sigma, i \rightarrow j} = \mathcal{S}\mathcal{X}\mathcal{B}_{\sigma, i \rightarrow j} I_{\sigma, i \rightarrow j}. \qquad (13)$$

This equation allows us to identify the ionization events per photon – coefficient S/XB (for only one metastable σ) as:

$$\mathcal{S}\mathcal{X}\mathcal{B}_{\sigma, i \rightarrow j} = \frac{S_\sigma}{A_{ij} \mathcal{F}_{i\sigma}} . \qquad (14)$$

Equation (14) implicitly captures the general dependence of the S/XB coefficients on plasma parameters. As the name

suggests (and will be shown below), the S/XBs are proportional to the ionization rates and inversely proportional to the excitation rates. This roughly determines their dependence on electronic temperature: while both rates increase with temperature in the relevant ranges, the effect of ionization on temperature is more pronounced. Consequently, the coefficients tend to exhibit a monotonic increase with temperature. Concerning their dependence on electron density, the S/XB coefficients appear to be independent of density at low values. At intermediate density values, the relationship becomes cumbersome, as the excitations occur through an effective rate $\mathcal{F}$ described in expression (12), which requires solving a complex collisional-radiative problem that accounts for all cascade processes.

3.3. Derivation of S/XB formula for many metastables

Transitions from metastables can compete with the direct excitation from the ground state as the population processes for the upper transition levels. That happens even for low electronic densities and also even for small metastable populations. Therefore, we need to reconsider equation (13) for *metastable cross-coupling*. First of all, if we have τ metastables, we need to measure the emissivity of $(n = \tau)$ different lines

$$I_1 = I_i \equiv I_{\sigma\rho\cdots\tau, i \rightarrow j} = \int_0^\infty A_{ij} n_i(\xi)\, d\xi$$
$$I_2 = I_l \equiv I_{\sigma\rho\cdots\tau, l \rightarrow m} = \int_0^\infty A_{lm} n_l(\xi)\, d\xi$$
$$\cdots$$
$$I_n = I_s \equiv I_{\sigma\rho\cdots\tau, s \rightarrow t} = \int_0^\infty A_{st} n_s(\xi)\, d\xi$$

in which the subscripts $\sigma\rho\cdots\tau$ indicate that, in principle, all the upper levels $i, l, \cdots, s$ can be populated by excitations from all the metastables, namely,

$$n_i = n_e n_\sigma \mathcal{F}_{i\sigma} + n_e n_\rho \mathcal{F}_{i\rho} + \cdots + n_e n_\tau \mathcal{F}_{i\tau}$$
$$n_l = n_e n_\sigma \mathcal{F}_{l\sigma} + n_e n_\rho \mathcal{F}_{l\rho} + \cdots + n_e n_\tau \mathcal{F}_{l\tau}$$
$$\cdots$$
$$n_s = n_e n_\sigma \mathcal{F}_{s\sigma} + n_e n_\rho \mathcal{F}_{s\rho} + \cdots + n_e n_\tau \mathcal{F}_{s\tau} \qquad (15)$$

which, in matrix form is written as:

$$\frac{1}{n_e}(\vec{n}_k) = (\mathbf{F})\,(\vec{n}_\mu) , \qquad (16)$$

where the reduced *n*-dimensional column vectors and the corresponding $n \times n$ operators are

$$(\vec{n}_k) \equiv \begin{pmatrix} n_i \\ n_l \\ \cdots \\ n_s \end{pmatrix}; \; (\vec{n}_\mu) \equiv \begin{pmatrix} n_\sigma \\ n_\rho \\ \cdots \\ n_\tau \end{pmatrix};$$

$$(\mathbf{F}) \equiv \begin{pmatrix} \mathcal{F}_{i\sigma} & \mathcal{F}_{i\rho} & \cdots & \mathcal{F}_{i\tau} \\ \mathcal{F}_{l\sigma} & \mathcal{F}_{l\rho} & \cdots & \mathcal{F}_{l\tau} \\ \cdots & \cdots & \cdots & \cdots \\ \mathcal{F}_{s\sigma} & \mathcal{F}_{s\rho} & \cdots & \mathcal{F}_{s\tau} \end{pmatrix} . \qquad (17)$$

The population numbers of the metastable levels n_σ and n_ρ are:

$$\left(\vec{n}_\mu\right) = \frac{1}{n_e} \left(\mathbf{F}\right)^{-1} \left(\vec{n}_k\right) = \frac{1}{n_e} \left(\mathbf{R}\right) \left(\vec{n}_k\right), \tag{18}$$

in which the inverse of the reduced matrix $(\mathbf{F})$ is denoted as

$$\left(\mathbf{R}\right) \equiv \left(\mathbf{F}\right)^{-1}.$$

The total flux is

$$\begin{aligned}
\Gamma &= \Gamma_\sigma + \Gamma_\rho + \cdots + \Gamma_\tau \\
&\approx n_e S_\sigma \int_0^\infty n_\sigma + n_e S_\rho \int_0^\infty n_\rho + \cdots + n_e S_\tau \int_0^\infty n_\tau \\
&= S_\sigma \int_0^\infty \left(\mathcal{R}_{\sigma i} n_i + \mathcal{R}_{\sigma l} n_l + \cdots + \mathcal{R}_{\sigma s} n_s\right) \\
&\quad + S_\rho \int_0^\infty \left(\mathcal{R}_{\rho i} n_i + \mathcal{R}_{\rho l} n_l + \cdots + \mathcal{R}_{\rho s} n_s\right) \\
&\quad + \cdots + S_\tau \int_0^\infty \left(\mathcal{R}_{\tau i} n_i + \mathcal{R}_{\tau l} n_l + \cdots \mathcal{R}_{\tau n} n_n\right) \\
&\approx \frac{1}{A_{ij}} \left(S_\sigma \mathcal{R}_{\sigma i} + S_\rho \mathcal{R}_{\rho i} + \cdots + S_\tau \mathcal{R}_{\tau i}\right) \\
&\quad \times \int_0^\infty A_{ij} n_i + \frac{1}{A_{lm}} \sum_{\mu=\sigma}^\tau S_\mu \mathcal{R}_{\mu l} \times I_l + \cdots + \\
&\quad + \frac{1}{A_n} \sum_{\mu=\sigma}^\tau S_\mu \mathcal{R}_{\mu n} \times I_n = \sum_{k=1}^n \mathcal{SXB}_k \times I_k \tag{19}
\end{aligned}$$

where $A_n \equiv A_{st}$ and

$$\begin{aligned}
\mathcal{SXB}_k &\equiv \sum_\mu \mathcal{SXB}_{\mu k} = \frac{1}{A_k} \sum_\mu S_\mu \mathcal{R}_{\mu k} \\
&= \frac{1}{A_k} \sum_\mu S_\mu \left(\mathbf{F}\right)_{\mu k}^{-1}. \tag{20}
\end{aligned}$$

3.4. Calculational methods

We carried out an evaluation of the atomic structure, as well as the collisional and radiative rates required to solve the collisional-radiative problem, using three separate independent calculations. Specifically, we utilized the atomic structure codes Hebrew University—Lawrence Livermore Atomic Code (HULLAC) [28, 29], the AutoStructure (AS) code [30–32], and the flexible atomic code (FAC) [33]. Since these three codes are well-established in both astrophysical and fusion research, we will only provide a brief overview of their key features.

The HULLAC code is a fully relativistic atomic structure package that computes transition energies and corresponding rate coefficients, among other quantities. It employs a relativistic potential method to solve the Dirac Hamiltonian and uses full multiconfiguration wavefunctions to calculate radiative transition rates. Configuration mixing, and hence correlation effects, are included in the calculations. The Breit interaction and quantum electrodynamics corrections (vacuum polarization and self-energy) are treated as second-order perturbations.

The AS code is used to compute energy levels, oscillator strengths, excitation and photoionization cross sections, as well as autoionization rates, among other properties. These can be calculated at different levels of resolution: configuration resolution (configuration average, CA), term resolution (LS coupling), or level resolution (intermediate coupling, IC), utilizing semi-relativistic, kappa-averaged wavefunctions. The code also allows for the inclusion of configuration mixing.

Finally, the FAC code uses a fully relativistic approach to solve the Dirac equation. Quantum electrodynamics effects, primarily arising from the Breit interaction, vacuum polarization, and electron self-energy, are included in the standard procedures of the code. Like the other programs mentioned, FAC has been extensively used for interpreting spectroscopic data in both laboratory and astrophysical contexts.

4. Results

4.1. Atomic structure

The ion W^{5+} is isoelectronic to Thulium ($Z = 69$), having a ground configuration [Xe] $4f^{14}5d$. This configuration has two levels separated by about 1 eV of energy. The lowest level of the ground configuration is $(4f^{14}5d)_{\frac{3}{2}}$ and the second level is $(4f^{14}5d)_{\frac{5}{2}}$. For most of the relevant electronic densities and temperatures, both of these two levels are significantly occupied and in particular, the population of the $J = \frac{5}{2}$ is higher than those of the ground level. We found two radiative transitions well separated and distinguishable in the experimental spectra, corresponding to the $(4f^{14}5f)_{\frac{5}{2}} \rightarrow (4f^{14}5d)_{\frac{3}{2}}$ transition at $\lambda_1 = 382.13$ Å, and $(4f^{14}5f)_{\frac{7}{2}} \rightarrow (4f^{14}5d)_{\frac{5}{2}}$ transition at $\lambda_1 = 394.07$ Å.

We include in our calculations, the $4f^{14}5l$ ($l = 2 - 4$), $4f^{14}6l$ ($l = 0 - 4$), and $4f^{14}7l$ ($l = 0 - 4$). We also include configuration-interaction (CI) between those configurations and $4f^{13}5d^2$, $4f^{13}5d6s$, $4f^{13}5d6p$, $4f^{13}6s^2$, $4f^{13}6s6p$, and also with the open 5p-shell $4f^{14}5p^5 5d^2$, $4f^{14}5p^5 5d6s$, $4f^{14}5p^5 6s^2$, $4f^{14}5p^5 5d6p$, and $4f^{14}5p^5 6s6p$. This structure conforms to a total of 436 levels, the model used in HULLAC calculations. Excluding the last $4f^{14}5p^5 6s6p$ configuration, the structure has 430 levels, and this is the model used for the AS and FAC calculations. We show in table 1 the detailed results obtained with the three different calculations only for the four levels involved in the transitions.

Figure 3 shows the spectra observed from EAST discharge (#100 300) at a time $t = 5.200$ s, corresponding to the maximum of the W burst. The figure also includes our three

Table 1. Atomic structure for the four-levels of W^{5+} involved in the 382.13 Å and the 394.07 Å transitions.

Index	*E* (eV)			Level
	HULLAC	AS	FAC	
1	0.0000	0.0000	0.0000	$(4f^{14}5d)_{3/2}$
2	0.9718	1.3653	1.0142	$(4f^{14}5d)_{5/2}$
3	31.769	31.823	31.729	$(4f^{14}5f)_{5/2}$
4	31.841	31.973	31.814	$(4f^{14}5f)_{7/2}$
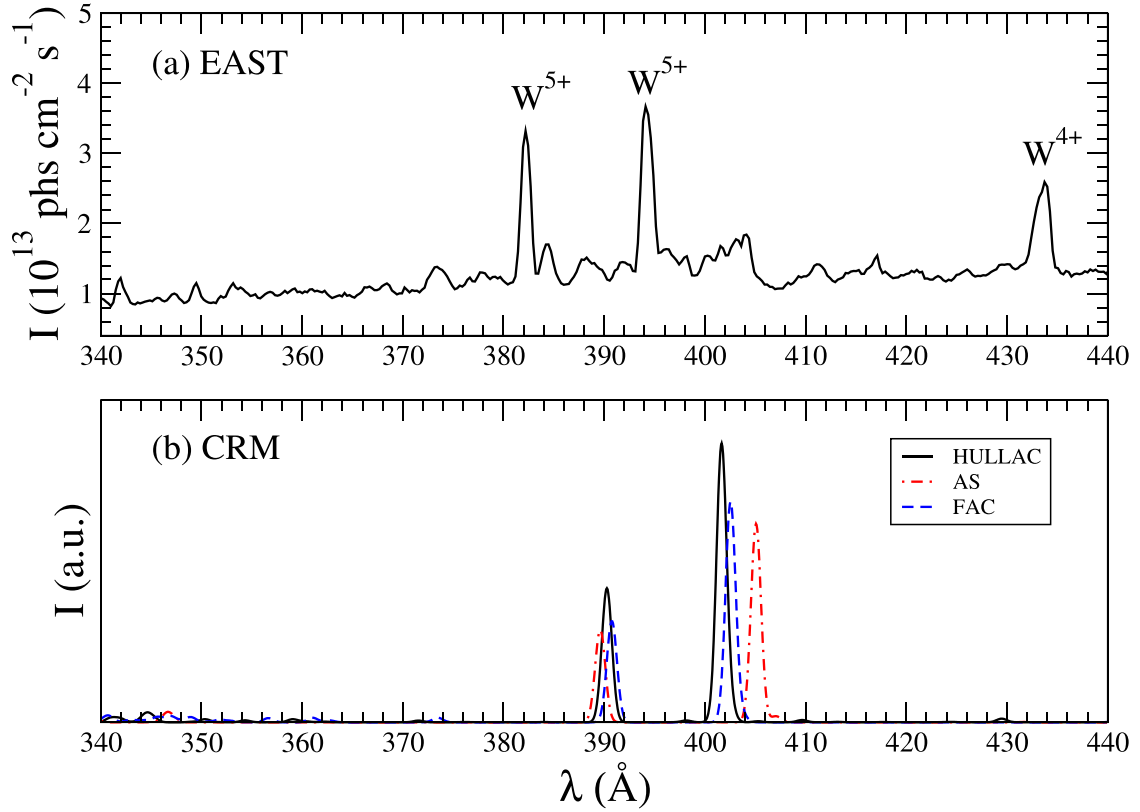
Figure 3. EAST spectrum and theoretical collisional-radiative synthetic spectra for the $5f \rightarrow 5d$ transitions of the W^{5+} ion. Upper graph: EAST Experimental spectra (#100 300, at $t = 5.200$ s). Lower graph: synthetic spectra calculated with HULLAC, AS, and FAC.

independent W^{5+} synthetic spectra, which were obtained by solving the fully collisional-radiative model.

As the figure shows, the agreement between the three theoretical calculations is satisfactory, although the results are consistently higher than the experimental values by about 7 Å. Surprisingly, another simpler calculation, including only 20 levels from the $4f^{14}5p^{6}5l$ ($l = 2 - 4$), $4f^{14}5p^{6}6l$ ($l = 0 - 3$), and $4f^{14}5p^{6}7l$ ($l = 0 - 3$) configurations produces transition energies much closer to the experimental values, above the experimental for only 2 Å, in all three cases. However, these calculations do not take into account the configuration mixings between the $4f^{14}5f$ and the $4f^{13}5d^2$ configurations, which account for a total mixing of about 11% for both the $J = 5/2$ and $J = 7/2$ levels. This indicates that the latter model cannot be considered valid, and some serendipity is being introduced, which deserves to be investigated in the future.

4.2. Excitation and radiative rates

The three codes have been employed to calculate the electron-impact excitation rate coefficients. They use the distorted-waves approximation, which has been quite successful in determining excitation cross-sections for highly ionized species, where the effects of correlations are usually not significant. For W^{5+}, the coupling in the continuum is sufficiently small to allow the use of this approximation with reasonable accuracy. The overall agreement between the three codes is about 40%, for the range $20 < T_e < 100$ eV.

We also have calculated the radiative transition rate coefficients with the three codes, obtaining values that agree 20% for the dipole-allowed transitions. The values of the radiative transitions and the electron-impact excitation rate coefficients for the four levels involved in the $5f \rightarrow 5d$ lines are listed in table 2, for HULLAC, AS, and FAC calculations.

Table 2. Radiative transitions A and electron-impact excitation rate coefficients (in cm^{3}s^{-1}) for the four levels involved in the W^{5+} lines.

			HULLAC					
			T_e (eV)					
Lower	Upper	A (s^{-1})	20	40	60	80	90	100
1	2	$5.20 \times 10^{+00}$	3.78×10^{-09}	2.47×10^{-09}	1.89×10^{-09}	1.56×10^{-09}	1.45×10^{-09}	1.35×10^{-09}
1	3	$1.61 \times 10^{+10}$	3.36×10^{-09}	5.88×10^{-09}	6.84×10^{-09}	7.27×10^{-09}	7.40×10^{-09}	7.49×10^{-09}
2	3	$1.16 \times 10^{+09}$	4.54×10^{-10}	6.56×10^{-10}	6.80×10^{-10}	6.68×10^{-10}	6.59×10^{-10}	6.49×10^{-10}
1	4	$1.01 \times 10^{+01}$	3.29×10^{-10}	4.27×10^{-10}	4.01×10^{-10}	3.62×10^{-10}	3.44×10^{-10}	3.27×10^{-10}
2	4	$1.83 \times 10^{+10}$	3.92×10^{-09}	6.66×10^{-09}	7.65×10^{-09}	8.09×10^{-09}	8.21×10^{-09}	8.30×10^{-09}
3	4	2.18×10^{-03}	4.91×10^{-09}	3.15×10^{-09}	2.42×10^{-09}	2.02×10^{-09}	1.87×10^{-09}	1.75×10^{-09}

			AUTOSTRUCTURE					
			T_e (eV)					
Lower	Upper	A (s^{-1})	20	40	60	80	90	100
1	2	$1.44 \times 10^{+01}$	8.62×10^{-09}	4.81×10^{-09}	3.36×10^{-09}	2.61×10^{-09}	2.35×10^{-09}	2.15×10^{-09}
1	3	$1.64 \times 10^{+10}$	2.74×10^{-09}	4.94×10^{-09}	5.89×10^{-09}	6.37×10^{-09}	6.52×10^{-09}	6.63×10^{-09}
2	3	$1.08 \times 10^{+09}$	4.50×10^{-10}	6.14×10^{-10}	6.27×10^{-10}	6.16×10^{-10}	6.08×10^{-10}	6.00×10^{-10}
1	4	$1.04 \times 10^{+01}$	3.63×10^{-10}	4.36×10^{-10}	3.96×10^{-10}	3.53×10^{-10}	3.34×10^{-10}	3.17×10^{-10}
2	4	$1.71 \times 10^{+10}$	3.34×10^{-09}	5.76×10^{-09}	6.74×10^{-09}	7.22×10^{-09}	7.36×10^{-09}	7.47×10^{-09}
3	4	2.02×10^{-02}	1.01×10^{-08}	5.46×10^{-09}	3.79×10^{-09}	2.95×10^{-09}	2.67×10^{-09}	2.44×10^{-09}

			FAC					
			T_e (eV)					
Lower	Upper	A (s^{-1})	20	40	60	80	90	100
1	2	$5.90 \times 10^{+00}$	5.07×10^{-09}	3.19×10^{-09}	2.40×10^{-09}	1.96×10^{-09}	1.81×10^{-09}	1.68×10^{-09}
1	3	$1.28 \times 10^{+10}$	2.41×10^{-09}	4.27×10^{-09}	5.00×10^{-09}	5.35×10^{-09}	5.46×10^{-09}	5.54×10^{-09}
2	3	$9.40 \times 10^{+08}$	4.31×10^{-10}	6.04×10^{-10}	6.16×10^{-10}	5.98×10^{-10}	5.87×10^{-10}	5.76×10^{-10}
1	4	$9.29 \times 10^{+00}$	3.39×10^{-10}	4.31×10^{-10}	3.99×10^{-10}	3.56×10^{-10}	3.36×10^{-10}	3.18×10^{-10}
2	4	$1.50 \times 10^{+10}$	3.11×10^{-09}	5.33×10^{-09}	6.16×10^{-09}	6.53×10^{-09}	6.64×10^{-09}	6.72×10^{-09}
3	4	3.72×10^{-03}	5.70×10^{-09}	3.39×10^{-09}	2.57×10^{-09}	2.14×10^{-09}	1.99×10^{-09}	1.86×10^{-09}

4.3. Electron-impact ionization rates

For the calculation of the electron-impact ionization rate coefficients, we used the distorted-waves approximation. However, even by using this relatively simple approach, the calculations are cumbersome. First, the total direct ionization cross section σ^{DI} from the ground configuration levels involves the sum of the contribution of the ionization of the $4f$, $5s$, $5p$, and $5d$ subshells-electrons:

$$
e^- + [Kr]4d^{10}5s^25p^64f^{14}5d \rightarrow [Kr]4d^{10}\left\{\begin{array}{l} 5s^25p^64f^{14} \\ 5s^25p^64f^{13}5d \\ 5s^25p^54f^{14}5d \\ 5s5p^64f^{14}5d \end{array}\right\} + 2e^-.
$$

(21)

Second, the indirect pathway to ionization, through inner-shell excited intermediate levels must be taken into consideration since the cross-sections of these processes are much higher than the corresponding to the direct ionization, as indicated in the experimental ionization measurements by Stenke *et al* [34] and by Spruck *et al* [35]. The total cross-section σ_C^{EA}

for excitation-autoionization from an initial level g, to any final level k of the following ion, through inner-shell excitation to any intermediate autoionizing level j within a given configuration or complex C is given by [36]

$$
\sigma_C^{\mathrm{EA}}(E) = \sum_{j \in C} \sigma_{gj}(E) \left[\frac{\sum_k A_{jk}^a + \sum_i A_{ji} B_i^a}{\sum_k A_{jk}^a + \sum_i A_{ji}}\right]
$$
$$
\equiv \sum_{j \in C} \sigma_{gj}(E) B_j^a
$$

(22)

where $\sigma_{gj}(\mathrm{E})$ is the cross section for electron-impact excitation from g to j as a function of the incident electron kinetic energy E. A_{jk}^a is the rate coefficient for autoionization from j to k, and A_{ji} is the Einstein coefficient for spontaneous emission from j to any lower-lying level i. B_j^a is the multiple branching ratio for autoionization from level j, defined by the bracket term. This term contains, in turn, the effective branching ratio B_i^a for further autoionization from level i, defined by a similar recursive expression [36]. The total excitation-autoionization
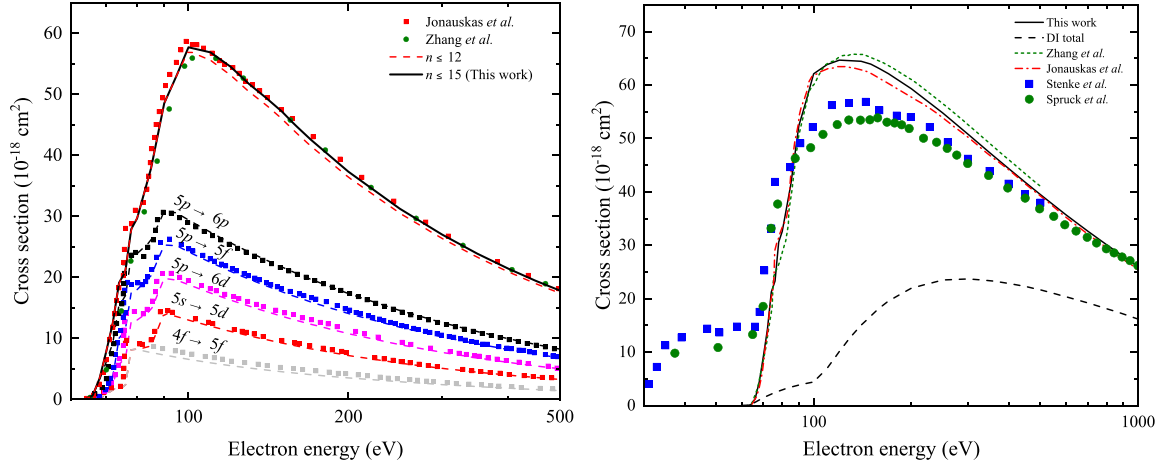
Figure 4. Left: excitation-autoionization cross-sections from the ground state of W^{5+}. Color-dashed lines: Present calculations of the accumulated partial EA cross sections σ_C^{EA} for the principal manifolds C. Color squares: theoretical results from Jonauskas *et al* [37]. Red circles: total theoretical results by Zhang *et al* [38]. Black-solid lines: present calculations for total σ^{EA}, considering $n \leqslant 15$. Right: total ionization cross-sections from the ground level. Black solid line: present calculations of the total ionization cross-section σ^{EIA} (equation (25)). Black-dashed line: total direct-ionization cross-section σ^{DI}. Green-dashed line: theoretical results from Jonauskas *et al* [37]. Red-dot dashed line: calculations by Zhang *et al* [38]. Blue squares: experimental results of Stenke *et al* [34]; Green circles: experimental results of Spruck *et al* [35].
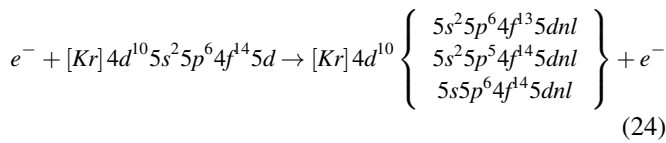
Table 3. Total ionization rate coefficients from the metastable levels of W^{5+}, in $\mathrm{cm}^3\mathrm{s}^{-1}$.

Metastable	T_e (eV)					
	20	40	60	80	90	100
1	2.01×10^{-09}	1.15×10^{-08}	2.04×10^{-08}	2.70×10^{-08}	2.96×10^{-08}	3.18×10^{-08}
2	2.07×10^{-09}	1.18×10^{-08}	2.08×10^{-08}	2.75×10^{-08}	3.01×10^{-08}	3.23×10^{-08}

cross-section is given by

$$\sigma^{\mathrm{EA}}(E) = \sum_C \sigma_C^{\mathrm{EA}}(E) . \tag{23}$$

In our calculation, we include excitations from the $4f$, $5p$, and $5s$ subshells of the ground configuration. These excitations are graphically represented as follows:

$$e^- + [Kr]4d^{10}5s^25p^64f^{14}5d \rightarrow [Kr]4d^{10} \left\{ \begin{array}{l} 5s^25p^64f^{13}5dnl \\ 5s^25p^54f^{14}5dnl \\ 5s5p^64f^{14}5dnl \end{array} \right\} + e^- \tag{24}$$

where we take all the possibles $5 \leqslant n \leqslant 15$ and $l \leqslant 4$.

In a low-ionized species such as W^{5+}, the radiative rates from the doubly excited levels are quite small compared to the autoionizing rates. Therefore, we can neglect the multiple branching ratios in (22). In that way, we assume that once the excited electron reaches an autoionizing level, it autoionizes and does not follow further cascades.

The total electron-impact single ionization cross-section is

$$\sigma^{\mathrm{EIA}}(E) = \sigma^{\mathrm{DI}}(E) + \sigma_C^{\mathrm{EA}}(E) . \tag{25}$$

Since the calculations are demanding, we only use one computational code for the ionization cross-section results.

Also, for comparisons with other calculations, we choose to use the FAC code. In figure 4, we show the contribution of the different channels to the electron-impact ionization cross-sections of W^{5+}. In the left part of the figure, we concentrate on the indirect excitation-autoionization channels σ^{EA}. The figure shows the accumulated contribution from the essential manifolds (dashed-color curves), together with the theoretical values reported by Jonauskas *et al* [37]. The results are in excellent agreement and the slight differences can be attributed to the lack of some configuration interactions that we have not included in the calculations. On the other hand, Jonauskas *et al* calculated the EA contribution up to the $n = 12$ manifold, whereas we also included the $n = (14, 15)$ configurations.

In the right part of the figure, the total ionization cross-sections σ^{EIA} are displayed. We intended to show the individual contribution of the ionization from the ground level $(4f^{14}5d)_{\frac{3}{2}}$ and from the metastable $(4f^{14}5d)_{\frac{5}{2}}$, but both cross-sections are very similar and are not easily distinguishable in the graph. The figure shows our results, together with the theoretical calculations reported by Jonauskas *et al* [37] and also the results given by Zhang *et al* [38]. As expected, the agreement is excellent. The differences can be attributed to the configurations used in the potential optimization and the configurations considered for the mixing interactions. To be able to assess the importance of the indirect channels, we include in the figure the total direct ionization σ^{DI} in dashed lines. The
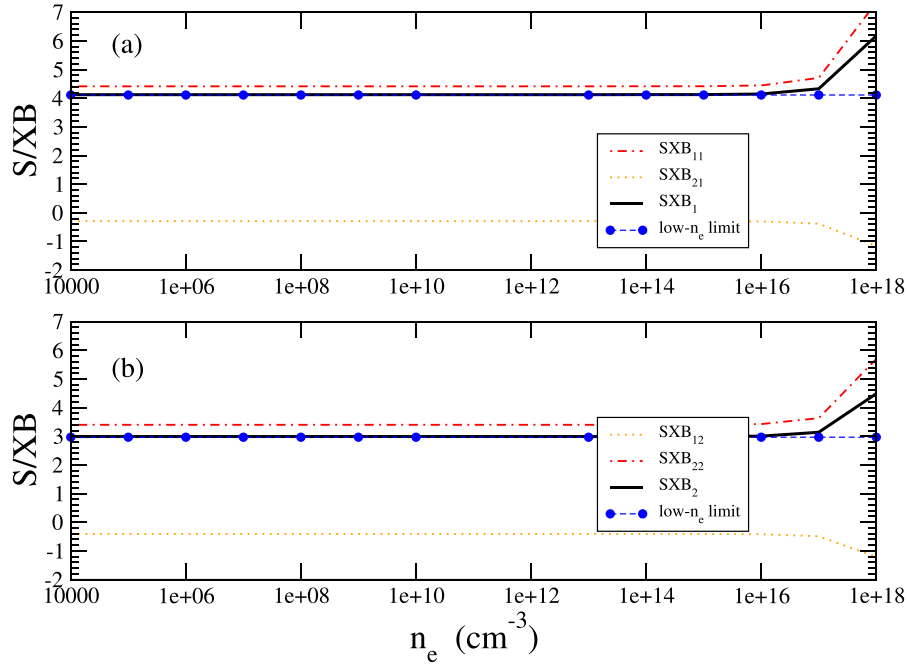
Figure 5. S/XB coefficients, according to the definition in equation (20), for a four-level model. (*a*) S/XB for the $3 \to 1$ transition $((4f^{14}5f)_{5/2} \to (4f^{14}5d)_{3/2})$. (*b*) $4 \to 2$ transition $((4f^{14}5f)_{7/2} \to (4f^{14}5d)_{5/2})$, in W^{5+}. The electronic temperature is $T_e = 60$ eV. The low-density limit curves correspond to the approximation given in equation (26).

figure also shows the experimental results given by Stenke *et al* [34], and more recent calculations from Spruck *et al* [35]. The distorted-waves are known for generally overestimation of the cross-sections. Both experimental results show a high presence of metastable contributions, so the discrepancies between theoretical and experimental results could be even more significant. The total ionization rate coefficients for each metastable state, derived from assuming a Maxwellian electronic distribution, are presented in table 3.

4.4. S/XB results

4.4.1. Simple model (four-levels). We found that a simple model having only four levels, namely, the ground level $(4f^{14}5d)_{3/2}$, the metastable $(4f^{14}5d)_{5/2}$, and the two upper-excited levels, $(4f^{14}5f)_{5/2}$ and $(4f^{14}5f)_{7/2}$, can be used to explain qualitatively many of the basic features in the determination of impurity flux. A detailed derivation of the S/XB partial coefficients is given in the appendix. The final expressions for these coefficients are given in equation (A.17).

We show, in figure 5, the S/XB coefficients corresponding to the transition $3 \to 1$ (upper part (*a*)), and in the lower part (*b*), the coefficients corresponding to the $4 \to 2$ transition. The coefficients for this figure have been calculated using the rates obtained with FAC code for a typical electronic temperature $T_e = 60$ eV. As is expected, due to the high population of the metastable, the leading terms are the diagonal $\mathcal{SXB}_{11}$ and $\mathcal{SXB}_{22}$, being the cross terms a small negative contribution.

We can perform a further approximation, focusing on the low-density region, in order to understand the overall behavior of the S/XB coefficients. In this approximation, we neglect first the collisional decays that are proportional to the

electron density and compete with stronger radiative decays. We also make use of the rates listed in table 2, neglecting the relatively small terms, for example, $(A_{41} + A_{42} + A_{43}) \approx A_{42}$. Under these assumptions, the low-density limit expressions for the S/XB coefficients are

$$\mathcal{SXB}_{11} \approx \frac{S_1}{Q_{13} \frac{A_{31}}{A_{31} + A_{32}}}$$

$$\mathcal{SXB}_{21} \approx -\frac{S_2}{Q_{24} \frac{Q_{13}}{Q_{14}}}$$

$$\mathcal{SXB}_{12} \approx -\frac{S_1}{Q_{13} \frac{Q_{24}}{Q_{23}}}$$

$$\mathcal{SXB}_{22} \approx \frac{S_2}{Q_{24}} \tag{26}$$

which are all density independent. As is shown in figure 5, the approximated S/XB results are in excellent agreement with the exact expressions given in (A.17). The results of this approximation not only match the exact results at low electronic densities but this agreement is still maintained for densities that are above the standard operating values, even up to values such as $n_e \approx 10^{17}$ cm^{-3}.

We made comparisons between the S/XB coefficients resulting from the three independent calculations from HULLAC, AS, and FAC computational codes. The results are displayed in figure 6 for an electronic temperature $T_e = 60$ eV, and as before, the upper part shows the results for the $3 \to 1$ transition, and the lower part $4 \to 2$.

The same results are shown in figure 7 for the electronic density $n_e = 10^{13}$ cm^{-3}, which is within the normal range of operation in the EAST plasmas. The discrepancies between
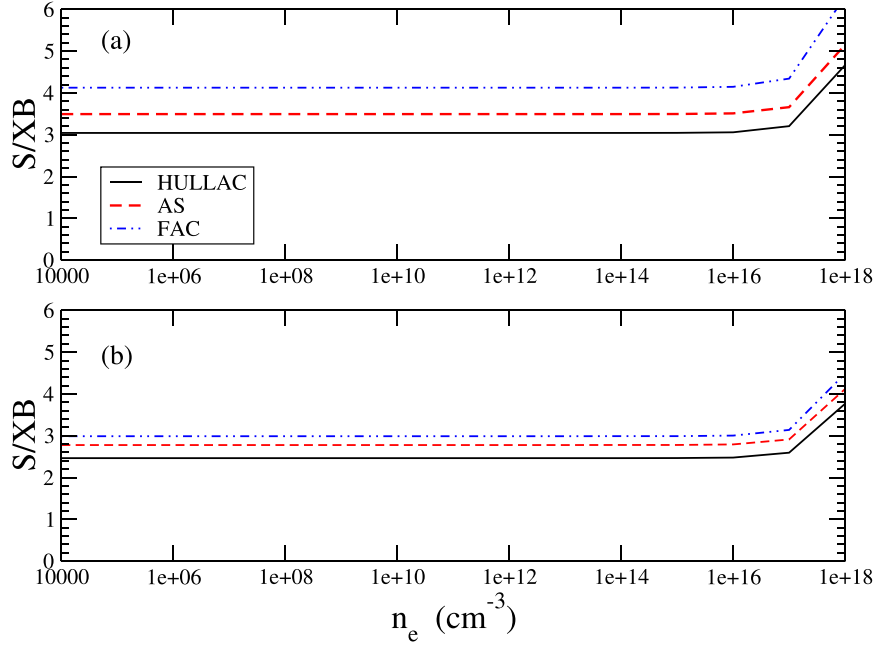
Figure 6. Comparisons of the S/XB coefficients obtained with the three independent calculations using HULLAC, AS, and FAC codes for the four-level model. (*a*) S/XB for the $3 \rightarrow 1$ transition ($(4f^{14}5f)_{5/2} \rightarrow (4f^{14}5d)_{3/2}$). (*b*) $4 \rightarrow 2$ transition ($(4f^{14}5f)_{7/2} \rightarrow (4f^{14}5d)_{5/2}$), in W^{5+}. The electronic temperature is $T_e = 60$ eV.
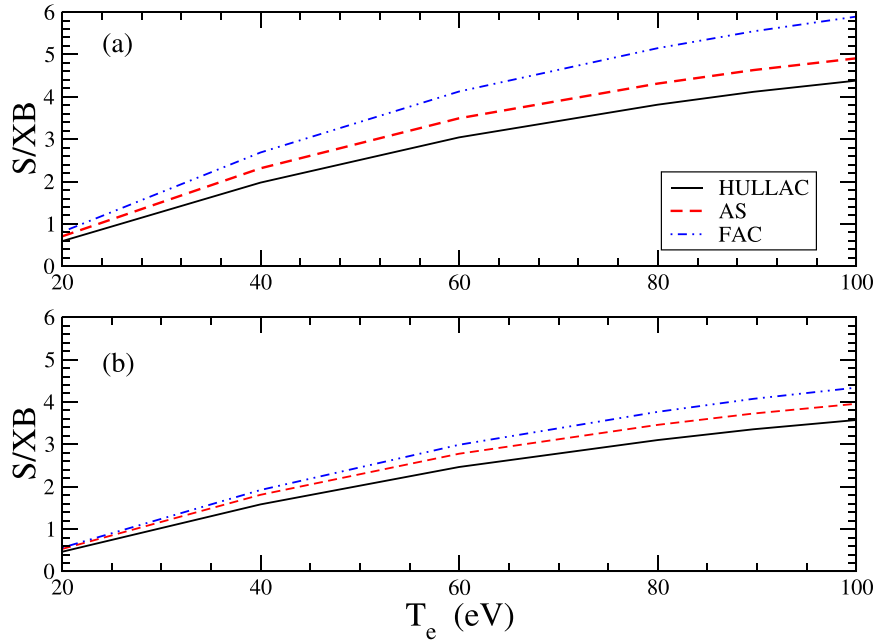

Figure 7. Comparisons of the S/XB coefficients obtained for the four-level model. (*a*) S/XB for the $3 \rightarrow 1$ transition ($(4f^{14}5f)_{5/2} \rightarrow (4f^{14}5d)_{3/2}$). (*b*) $4 \rightarrow 2$ transition ($(4f^{14}5f)_{7/2} \rightarrow (4f^{14}5d)_{5/2}$), in W^{5+}. The electronic density is $n_e = 10^{13}$ cm^{-3}.

the different calculations are consistent with the differences obtained for the values of the rates shown in table 2, in particular, for the A_{31} radiative decay rates.

4.4.2. Full model (430-levels). We included all the configurations listed in section 4.1 and solved the corresponding collisional-radiative equations, obtaining the S/XB ratios for

the same transitions studied previously. The results are displayed in figure 8 for a fixed electronic temperature $T_e = 60$ eV and in figure 9, for a fixed electronic density $n_e = 10^{13}$ cm^{-3}. We note that for both lines, the S/XB ratios appear nearly constant around an electron density from 10^4 cm^{-3}, to a density of approximately 10^{14} cm^{-3}. This justifies the previous approach in which we considered only four levels and the possibility of using the low-density approximation to obtain

a simple and quick determination of the incoming flux. At densities around $10^{15}\,\mathrm{cm^{-3}}$ the S/XB becomes sensitive to the collisional-radiative solutions. Therefore, we found substantial differences between the calculations, particularly between HULLAC results and the other two. Beyond $n_e > 10^{17}\,\mathrm{cm^{-3}}$, the plasma reaches the local thermodynamic equilibrium density regime, and then the S/XB ratios increase linearly with the density.

The detailed results for electronic densities in the range $10^4\,\mathrm{cm^{-3}} < n_e < 10^{18}\,\mathrm{cm^{-3}}$ and electronic temperatures in the range $20 < T_e < 100\,\mathrm{eV}$ are presented in tables 4–6 for the calculations realized with HULLAC, AS, and FAC, respectively. The agreement between the calculations for the $(4f^{14}5f)_{5/2} \to (4f^{14}5d)_{3/2}$ transition (the $3 \to 1$ transition in the four-level model) is of about 40% for $T_e = 50\,\mathrm{eV}$ and densities up to $n_e = 10^{15}\,\mathrm{cm^{-3}}$ in the worst case (HULLAC vs. FAC). Figure 9
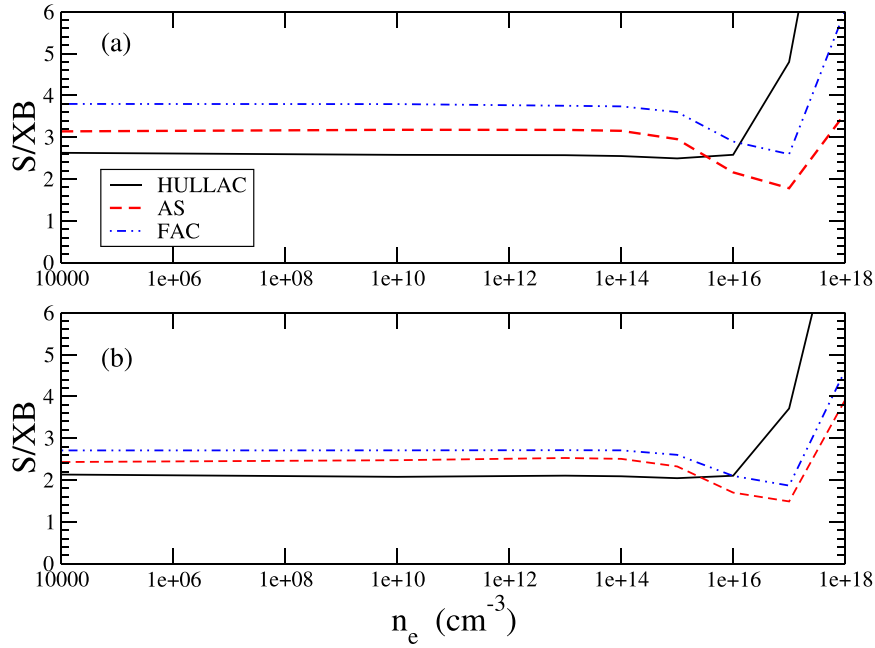

Figure 8. Comparisons of the S/XB coefficients obtained with the three independent calculations using HULLAC, AS, and FAC codes, for the 430-level model, in W^{5+}. (*a*) S/XB for the $(4f^{14}5f)_{5/2} \to (4f^{14}5d)_{3/2}$ transition. (*b*) $(4f^{14}5f)_{7/2} \to (4f^{14}5d)_{5/2}$ transition. The electronic temperature is $T_e = 60\,\mathrm{eV}$.
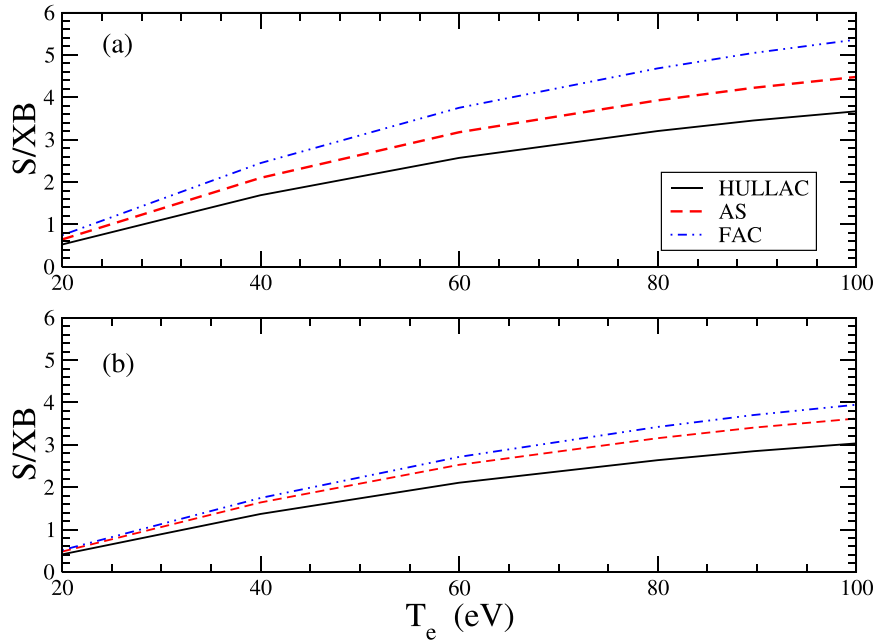

Figure 9. Comparisons of the S/XB coefficients obtained for the 430-level model, in W^{5+}. (*a*) S/XB for the $(4f^{14}5f)_{5/2} \to (4f^{14}5d)_{3/2}$ transition. (*b*) $(4f^{14}5f)_{7/2} \to (4f^{14}5d)_{5/2}$ transition. The electronic density is $n_e = 10^{13}\,\mathrm{cm^{-3}}$.

Table 4. SXB of W^{5+} for the radiative transitions (Line 1) $(4f^{14}5f)_{5/2} \rightarrow (4f^{14}5d)_{3/2}$, and (Line 2) $(4f^{14}5f)_{7/2} \rightarrow (4f^{14}5d)_{5/2}$, from a 436-level collisional-radiative model, calculated with the HULLAC computational suite.

Line	T_e(eV)	Electron density (cm^{-3})							
		10^4	10^{10}	10^{13}	10^{14}	10^{15}	10^{16}	10^{17}	10^{18}
1	20	0.543	0.532	0.525	0.519	0.502	0.504	0.804	1.710
	40	1.733	1.698	1.690	1.674	1.629	1.677	3.039	7.143
	60	2.626	2.577	2.569	2.549	2.492	2.579	4.798	11.90
	80	3.266	3.209	3.203	3.180	3.119	3.235	6.059	15.52
	90	3.516	3.458	3.452	3.429	3.367	3.494	6.543	16.92
	100	3.736	3.676	3.670	3.648	3.586	3.722	6.966	18.20
2	20	0.425	0.414	0.412	0.408	0.393	0.384	0.570	1.470
	40	1.391	1.354	1.367	1.355	1.318	1.331	2.258	5.758
	60	2.130	2.076	2.105	2.089	2.045	2.103	3.712	9.203
	80	2.661	2.598	2.636	2.620	2.575	2.678	4.805	11.70
	90	2.873	2.807	2.848	2.833	2.790	2.912	5.250	12.72
	100	3.056	2.988	3.032	3.017	2.975	3.116	5.639	13.60

Table 5. SXB of W^{5+} for the radiative transitions (Line 1) $(4f^{14}5f)_{5/2} \rightarrow (4f^{14}5d)_{3/2}$, and (Line 2) $(4f^{14}5f)_{7/2} \rightarrow (4f^{14}5d)_{5/2}$, from a 430-level collisional-radiative model, calculated with the AS computational code.

Line	T_e(eV)	Electron density (cm^{-3})							
		10^4	10^{10}	10^{13}	10^{14}	10^{15}	10^{16}	10^{17}	10^{18}
1	20	0.645	0.654	0.644	0.637	0.580	0.395	0.343	0.877
	40	2.076	2.107	2.099	2.080	1.921	1.352	1.136	2.457
	60	3.140	3.178	3.176	3.153	2.952	2.158	1.779	3.568
	80	3.889	3.927	3.928	3.905	3.694	2.787	2.272	4.356
	90	4.184	4.221	4.224	4.201	3.990	3.049	2.476	4.669
	100	4.442	4.476	4.480	4.457	4.249	3.285	2.657	4.929
2	20	0.469	0.480	0.479	0.474	0.430	0.293	0.249	0.674
	40	1.575	1.609	1.638	1.623	1.487	1.048	0.918	2.477
	60	2.431	2.474	2.526	2.507	2.326	1.699	1.487	3.913
	80	3.046	3.090	3.155	3.135	2.939	2.210	1.930	4.965
	90	3.293	3.336	3.404	3.385	3.186	2.425	2.115	5.390
	100	3.505	3.547	3.618	3.599	3.400	2.617	2.281	5.765

Table 6. SXB of W^{5+} for the radiative transitions (Line 1) $(4f^{14}5f)_{5/2} \rightarrow (4f^{14}5d)_{3/2}$, and (Line 2) $(4f^{14}5f)_{7/2} \rightarrow (4f^{14}5d)_{5/2}$, from a 430-level collisional-radiative model, calculated with the FAC computational code.

| Line	T_e(eV)	Electron density (cm^{-3})							
		10^4	10^{10}	10^{13}	10^{14}	10^{15}	10^{16}	10^{17}	10^{18}
1	20	0.762	0.759	0.745	0.740	0.696	0.529	0.484	1.328
	40	2.484	2.479	2.448	2.436	2.326	1.828	1.670	4.094
	60	3.796	3.792	3.752	3.737	3.601	2.896	2.595	6.026
	80	4.730	4.725	4.681	4.666	4.525	3.710	3.273	7.351
	90	5.096	5.091	5.045	5.031	4.892	4.046	3.550	7.873
	100	5.414	5.409	5.361	5.348	5.211	4.343	3.790	8.314
2	20	0.520	0.518	0.512	0.510	0.482	0.371	0.323	0.830
	40	1.748	1.747	1.745	1.741	1.660	1.311	1.173	2.975
	60	2.707	2.709	2.714	2.710	2.603	2.098	1.866	4.619
	80	3.407	3.411	3.421	3.419	3.301	2.702	2.384	5.764
	90	3.685	3.690	3.702	3.701	3.580	2.951	2.595	6.203
	100	3.926	3.932	3.945	3.946	3.824	3.173	2.780	6.579
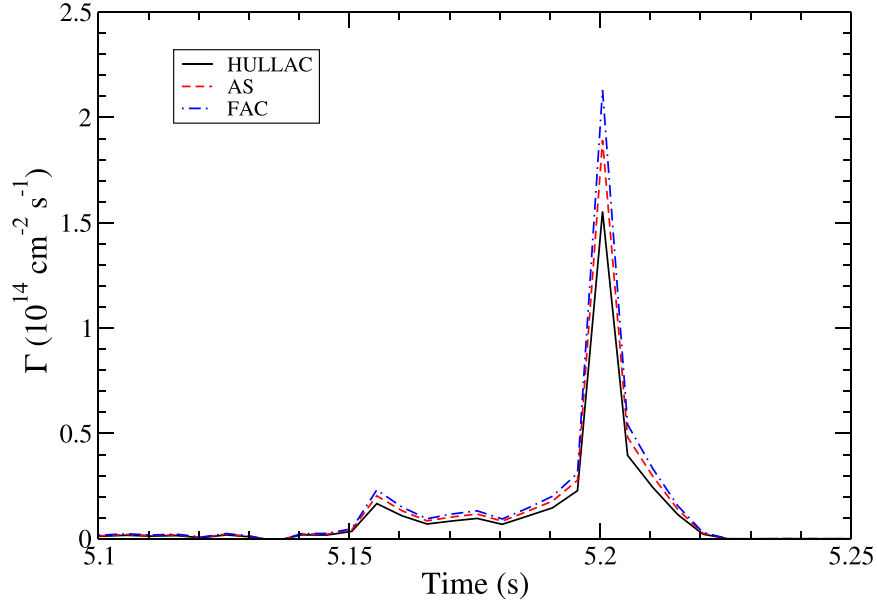
Figure 10. Total tungsten influx from the plasma-facing surface, calculated for the discharge #100 300 at EAST, as a function of time.

shows that the agreement is much better at lower temperatures. For the $(4f^{14}5f)_{7/2} \rightarrow (4f^{14}5d)_{5/2}$ transition, the agreement at $T_e = 50$ eV is about 25%, it is much better for lower temperatures.

4.5. Tungsten influx

The absolute calibration of the spectral line intensities [19–22] results in values of the $5f \rightarrow 5d$ transitions about 3×10^{13} photons per cm^2 per second at the emission peak corresponding to the tungsten burst. Assuming that the tungsten ions are sputtered from a region in which the electronic temperature is $T_e = 60$ eV and the electronic density is $n_e = 10^{13}$ cm^{-3}, the S/XB ratios are of the order of 3, we can infer a total tungsten flux of the order of 10^{14} particles per cm^2 per second at the peak. Indeed, we show in figure 10 the calculated total tungsten flux from the plasma-facing surface towards the interior of the EAST device, which follows the behavior of the line intensity in time for discharge #100 300, having a peak at $t = 5.2$ s. The fluxes are calculated using three independent calculations: HULLAC, AS, and FAC. The three calculations agree at the peak between 45% in the worst comparison case (HULLAC vs. FAC).

5. Conclusions

In this study, we derive the relevant equations for calculating the S/XB coefficients in scenarios where, rather than assuming a single initial state, multiple metastable states with significant populations and influence on ionization processes are considered. Unlike excited states, metastable states primarily equilibrate their populations with those of neighboring ions. This allows for the expression of the relative populations of the excited states in terms of the populations of the metastable states, without the need for explicitly specifying the latter's population values. Similarly, ionization events, which

are dependent on the metastable populations, can be described in terms of the radiative emissions from the excited states.

Extensive theoretical calculations of atomic structure, radiative decay, electron-impact excitation, and electron-impact ionization have been carried out to generate the data necessary to model the W^{5+} ion in a plasma environment. We use three different atomic computational codes – FAC, HULLAC, and AUTOSTRUCTURE – which allow us to assess the accuracy of our theoretical results. For the electron-impact ionization, we included contributions from excitation-autoionization processes up to $n = 15$ manifolds and calculated the rate coefficients for the total ionization from both the two $4f^{14}5d$ configuration levels.

Using these data, we solved a collisional-radiative model to obtain the effective population coefficients needed in to determine the S/XB ratios. We selected the radiative transitions $(4f^{14}5f)_{5/2} \rightarrow (4f^{14}5d)_{3/2}$ and $(4f^{14}5f)_{7/2} \rightarrow (4f^{14}5d)_{5/2}$, which are prominent in the 320–460 Å range. The process of radiative cascade from energy terms higher than the upper terms involved in the radiative transition was found to have a negligible effect on the S/XB ratios for both types of transitions at low and intermediate energy densities. Therefore, by using a simple four-level collisional-radiative model consisting of the two upper levels and the two lower metastables, we can generate S/XB ratios that agree very well with the 430-level model. That is particularly useful because it allows us to derive simple analytical expressions that help us understand the principal mechanisms contributing to the ionization.

Acknowledgments

Appendix. Derivation of S/XB coefficients for four-levels and two metastables

The collisional-radiative equations (2) for four-levels is:

$$
\begin{pmatrix} \frac{dn_1}{dt} \\ \frac{dn_2}{dt} \\ 0 \\ 0 \end{pmatrix} = \begin{pmatrix} C_{11} & C_{12} & C_{13} & C_{14} \\ C_{21} & C_{22} & C_{23} & C_{24} \\ C_{31} & C_{32} & C_{33} & C_{34} \\ C_{41} & C_{42} & C_{43} & C_{44} \end{pmatrix} \begin{pmatrix} n_1 \\ n_2 \\ n_3 \\ n_4 \end{pmatrix}, \quad (A.1)
$$

and for the excited-levels part of the matrix, the corresponding system of equations is

$$
\begin{pmatrix} C_{31}n_1 + C_{32}n_2 + C_{33}n_3 + C_{34}n_4 \\ C_{41}n_1 + C_{42}n_2 + C_{43}n_3 + C_{44}n_4 \end{pmatrix} = \begin{pmatrix} 0 \\ 0 \end{pmatrix} \quad (A.2)
$$

which is equivalent to

$$
\begin{pmatrix} C_{33}n_3 + C_{34}n_4 \\ C_{43}n_3 + C_{44}n_4 \end{pmatrix} = \begin{pmatrix} -C_{31}n_1 - C_{32}n_2 \\ -C_{41}n_1 - C_{42}n_2 \end{pmatrix}. \quad (A.3)
$$

In matrix form:

$$
\mathbf{C}_s \cdot \vec{n}_s = \vec{C}_1 \cdot n_1 + \vec{C}_2 \cdot n_2 \quad (A.4)
$$

where

$$
\vec{n}_s = \begin{pmatrix} n_3 \\ n_4 \end{pmatrix}, \quad (A.5)
$$

the reduced matrix for the excited levels is

$$
\mathbf{C}_s = \begin{pmatrix} C_{33} & C_{34} \\ C_{43} & C_{44} \end{pmatrix} \quad (A.6)
$$

and the column vectors are

$$
\vec{C}_1 = \begin{pmatrix} -C_{31} \\ -C_{41} \end{pmatrix} \quad (A.7)
$$

and

$$
\vec{C}_2 = \begin{pmatrix} -C_{32} \\ -C_{42} \end{pmatrix}. \quad (A.8)
$$

The solution for the excited levels is

$$
\begin{aligned} \vec{n}_s &= [\mathbf{C}_s]^{-1} \cdot \vec{C}_1 \cdot n_1 + [\mathbf{C}_s]^{-1} \cdot \vec{C}_1 \cdot n_1 \\ &= \vec{\mathcal{F}}_1 \cdot n_1 + \vec{\mathcal{F}}_2 \cdot n_2 \end{aligned} \quad (A.9)
$$

in which the column vectors are

$$
\vec{\mathcal{F}}_1 \equiv [\mathbf{C}_s]^{-1} \cdot \vec{C}_1 \quad \text{and} \quad \vec{\mathcal{F}}_2 \equiv [\mathbf{C}_s]^{-1} \cdot \vec{C}_2. \quad (A.10)
$$

The inverse of $\mathbf{C}_s$ is

$$
[\mathbf{C}_s]^{-1} = \frac{1}{C_{33}C_{44} - C_{34}C_{43}} \begin{pmatrix} C_{44} & -C_{34} \\ -C_{43} & C_{33} \end{pmatrix} \quad (A.11)
$$

and

$$
(\mathbf{F}) = \begin{pmatrix} \vec{\mathcal{F}}_1 & \vec{\mathcal{F}}_2 \end{pmatrix} \quad (A.12)
$$

becomes

$$
\begin{aligned} (\mathbf{F}) &= \frac{1}{C_{33}C_{44} - C_{34}C_{43}} \\ &\times \begin{pmatrix} -C_{31}C_{44} + C_{34}C_{41} & -C_{32}C_{44} + C_{34}C_{42} \\ C_{31}C_{43} - C_{33}C_{41} & C_{32}C_{43} - C_{33}C_{42} \end{pmatrix}. \end{aligned} \quad (A.13)
$$

The inverse of the reduced matrix is

$$
\begin{aligned} (\mathbf{R}) \equiv (\mathbf{F})^{-1} &= \frac{1}{C_{31}C_{42} - C_{32}C_{41}} \\ &\times \begin{pmatrix} C_{32}C_{43} - C_{33}C_{42} & C_{32}C_{44} - C_{34}C_{42} \\ -C_{31}C_{43} + C_{33}C_{41} & -C_{31}C_{44} + C_{34}C_{41} \end{pmatrix}. \end{aligned} \quad (A.14)
$$

From the definition (20) for the S/XB coefficients

$$
\mathcal{SXB}_{\mu k} \equiv \frac{1}{A_k} S_\mu \mathcal{R}_{\mu k} \quad (A.15)
$$

we obtain

$$
\begin{aligned} \mathcal{SXB} &= \frac{1}{C_{31}C_{42} - C_{32}C_{41}} \\ &\times \begin{pmatrix} \frac{S_1}{A_{31}}(C_{32}C_{43} - C_{33}C_{42}) & \frac{S_2}{A_{31}}(-C_{31}C_{43} + C_{33}C_{41}) \\ \frac{S_1}{A_{42}}(C_{32}C_{44} - C_{34}C_{42}) & \frac{S_2}{A_{42}}(-C_{31}C_{44} + C_{34}C_{41}) \end{pmatrix} \end{aligned} \quad (A.16)
$$

and replacing the corresponding elements of the matrix (equation (3)), we obtain finally the expressions for the S/XB coefficients

15

$$\mathcal{SXB}_{11} = \frac{n_\mathrm{e} S_1}{A_{31}} \frac{n_\mathrm{e} Q_{23}\, n_\mathrm{e} Q_{34} - n_\mathrm{e} Q_{24}\left(-A_{31} - A_{32} - n_\mathrm{e} Q_{31} - n_\mathrm{e} Q_{32} - n_\mathrm{e} Q_{34}\right)}{n_\mathrm{e} Q_{13} n_\mathrm{e} Q_{24} - n_\mathrm{e} Q_{14} n_\mathrm{e} Q_{23}} \tag{A.17}$$

$$\mathcal{SXB}_{21} = \frac{n_\mathrm{e} S_2}{A_{31}} \frac{-n_\mathrm{e} Q_{13}\, n_\mathrm{e} Q_{34} + n_\mathrm{e} Q_{14}\left(-A_{31} - A_{32} - n_\mathrm{e} Q_{31} - n_\mathrm{e} Q_{32} - n_\mathrm{e} Q_{34}\right)}{n_\mathrm{e} Q_{13} n_\mathrm{e} Q_{24} - n_\mathrm{e} Q_{14} n_\mathrm{e} Q_{23}}$$

$$\mathcal{SXB}_{12} = \frac{n_\mathrm{e} S_1}{A_{42}} \frac{n_\mathrm{e} Q_{23}\left(-A_{41} - A_{42} - A_{43} - n_\mathrm{e} Q_{41} - n_\mathrm{e} Q_{42} - n_\mathrm{e} Q_{43}\right) - n_\mathrm{e} Q_{24}\left(A_{43} + n_\mathrm{e} Q_{43}\right)}{n_\mathrm{e} Q_{13} n_\mathrm{e} Q_{24} - n_\mathrm{e} Q_{14} n_\mathrm{e} Q_{23}}$$

$$\mathcal{SXB}_{22} = \frac{n_\mathrm{e} S_2}{A_{42}} \frac{n_\mathrm{e} Q_{13}\left(A_{41} + A_{42} + A_{43} + n_\mathrm{e} Q_{41} + n_\mathrm{e} Q_{42} + n_\mathrm{e} Q_{43}\right) + n_\mathrm{e} Q_{14}\left(A_{43} + n_\mathrm{e} Q_{43}\right)}{n_\mathrm{e} Q_{13} n_\mathrm{e} Q_{24} - n_\mathrm{e} Q_{14} n_\mathrm{e} Q_{23}}.$$

ORCID iDs

Fengling Zhang https://orcid.org/0009-0008-0873-0071
Darío Mitnik https://orcid.org/0000-0003-0193-0958
Ling Zhang https://orcid.org/0000-0001-7880-9588
Wenmin Zhang https://orcid.org/0009-0000-9980-6765
Shigeru Morita https://orcid.org/0000-0003-4139-7721
Yunxin Cheng https://orcid.org/0000-0002-9195-2757
Xiaobin Ding https://orcid.org/0000-0003-0004-3206
Haiqing Liu https://orcid.org/0000-0001-6892-358X

References

[1] Behringer K., Summers H.P., Denne B., Forrest M. and Stamp M. 1989 Spectroscopic determination of impurity influx from localized surfaces *Plasma Phys. Control Fusion* **31** 2059

[2] Field A.R., Garcıa-Rosales C., Lieder G., Pitcher C.S. and Radtke R. 1996 Spectroscopic measurement of target plate erosion in the ASDEX Upgrade divertor *Nucl. Fusion* **36** 119

[3] Badnell N.R., Gorczyca T.W., Pindzola M.S. and Summers H.P. 1996 Excitation and ionization of neutral Cr and Mo and the application to impurity influx *J. Phys. B: At. Mol. Opt. Phys.* **29** 3683

[4] Griffin D.C., Pindzola M.S., Shaw J.A., Badnell N.R., O'Mullane M. and Summers H.P. 1997 Electron-impact excitation and ionization of Ar$^+$ for the determination of impurity influx in tokamaks *J. Phys. B: At. Mol. Opt. Phys.* **30** 3543

[5] Lipschultz B., Pappas D.A., LaBombard B., Rice J.E., Smith D. and Wukitch S.J. 2001 A study of molybdenum influxes and transport in Alcator C-Mod *Nucl. Fusion* **41** 585

[6] Coenen J.W. *et al* 2015 Materials for demo and reactor applications-boundary conditions and new concepts *Phys. Scr.* **T167** 014002

[7] Thoma A. *et al* 1997 Spectroscopic measurements of tungsten erosion in the ASDEX Upgrade divertor *Plasma Phys. Control. Fusion* **39** 1487

[8] Geier A., Maier H., Neu R. and Krieger K. (the ASDEX Upgrade Team) 2002 Determination of the tungsten divertor retention at ASDEX Upgrade using a sublimation probe *Plasma Phys. Control. Fusion* **44** 2091

[9] Nishijima D., Doerner R.P., Baldwin M.J., Pospieszczyk A. and Kreter A. 2011 Erratum: Experimental determination of S/XB values of W I visible lines *Phys. Plasma* **18** 019901

[10] Beigman I., Pospieszczyk A., Sergienko G., Tolstikhina I.Y. and Vainshtein L. 2007 Tungsten spectroscopy for the measurement of W-fluxes from plasma facing components *Plasma Phys. Control. Fusion* **49** 1833

[11] Pospieszczyk A., Borodin D., Brezinsek S., Huber A. Kirschner A., Mertens P., Sergienko G., Schweer B., Beigman I.L. and Vainshtein L. 2010 Determination of rate coefficients for fusion-relevant atoms and molecules by modelling and measurement in the boundary layer of textor *J. Phys. B: At. Mol. Opt. Phys.* **43** 144017

[12] Ballance C.P., Loch S.D., Pindzola M.S. and Griffin D.C. 2013 Electron-impact excitation and ionization of W^{3+} for the determination of tungsten influx in a fusion plasma *J. Phys. B: At. Mol. Opt. Phys.* **46** 055202

[13] Dong C.F. *et al* 2019 Evaluation of tungsten influx rate and study of edge tungsten behavior based on the observation of EUV line emissions from W^{6+} ions in HL-2A *Nucl. Fusion* **59** 016020

[14] Open-ADAS Atomic data and analysis structure (available at: https://open.adas.ac.uk)

[15] Wan B.N., Liang Y.F., Gong X.Z., Li J.G., Xiang N., Xu G.S., Sun Y.W., Wang L., Qian J.P. and Liu H.Q. 2017 Overview of EAST experiments on the development of high-performance steady-state scenario *Nucl. Fusion* **57** 102019

[16] Wan B.N., Liang Y., Gong X.Z., Xiang N., Xu G.S., Sun Y., Wang L., Qian J.P., Liu H.Q. and Zeng L. 2019 Recent advances in EAST physics experiments in support of steady-state operation for ITER and CFETR *Nucl. Fusion* **59** 112003

[17] Wang L. *et al* 2021 Progress of divertor heat and particle flux control in EAST for advanced steady-state operation in the last 10 years *J. Fusion Energy* **40** 1

[18] Wan B.N., Gong X.Z., Liang Y., Xiang N., Xu G.S., Sun Y., Wang L., Qian J.P., Liu H.Q. and Zhang B. 2022 Advances in the long-pulse steady-state high beta H-mode scenario with active controls of divertor heat and particle fluxes in EAST *Nucl. Fusion* **62** 042010

[19] Ling Z., Morita S., Zong X., Wu Z., Zhang P., Wu C., Gao W., Ohishi T., Goto M. and Shen J. 2015 A fast-time-response extreme ultraviolet spectrometer for measurement of impurity line emissions in the Experimental Advanced Superconducting Tokamak *Rev. Sci. Instrum.* **86** 123509

[20] Li L. *et al* 2021 Line identification of extreme ultraviolet (EUV) spectra from low-Z impurity ions in EAST tokamak plasmas *Plasma Sci. Technol.* **23** 075102

[21] Dong C., Morita S., Goto M. and Wang E. 2011 Absolute intensity calibration of flat-field space-resolved extreme ultraviolet spectrometer using radial profiles of visible and extreme ultraviolet bremsstrahlung continuum emitted from

high-density plasmas in large helical device *Rev. Sci. Instrum.* **82** 11

[22] Dong C., Morita S., Goto M. and Wang E. 2012 Extension of wavelength range in absolute intensity calibration of space-resolved EUV spectrometer for LHD diagnostics *Plasma Fusion Res.* **7** 2402139

[23] Han X. *et al* 2018 Multiple laser system for high-resolution Thomson scattering diagnostics on the EAST tokamak *IEEE Trans. Plasma Sci.* **46** 406

[24] Xu Q., Gao X., Jie Y., Liu H., Shi N., Cheng Y. and Tong X. 2008 HCN laser interferometer on the EAST superconducting tokamak *Plasma Sci. Technol.* **10** 519

[25] Duan Y., Hu L., Mao S., Xu P., Chen K., Lin S., Zhong G., Zhang J., Zhang L. and Wang L. 2011 Measurement of radiated power loss on EAST *Plasma Sci. Technol.* **13** 546

[26] Ling Zhang F. *et al* 2024 Line identification of extreme ultraviolet spectra from aluminum ions in EAST Tokamak plasmas *Phys. Scr.* **99** 025615

[27] Zhang W. *et al* 2024 First observation of edge impurity behavior with $n = 1$ RMP application in EAST L-mode plasma *Nucl. Fusion* **64** 086004

[28] Klapisch M., Schwob J.L., Fraenkel B.S. and Oreg J. 1977 The $1s - 3p$ Kβ-like x-ray spectrum of highly ionized iron *J. Opt. Soc. Am.* **67** 148

[29] Bar-Shalom A., Klapisch M. and Oreg J. 2001 HULLAC, an integrated computer package for atomic processes in plasmas *J. Quant. Spectrosc. Radiat. Transfer* **71** 169

[30] Badnell N.R. 1986 Dielectronic recombination of Fe^{22+} and Fe^{21+} *J. Phys. B: At. Mol. Opt. Phys.* **19** 3827

[31] Badnell N.R. 1997 On the effects of the two-body non-fine-structure operators of the Breit-Pauli Hamiltonian *J. Phys. B: At. Mol. Opt. Phys.* **30** 1–11

[32] Badnell N.R. 2011 A Breit-Pauli distorted wave implementation for AUTOSTRUCTURE *Comput. Phys. Commun.* **180** 1528

[33] Gu M.F. 2008 The flexible atomic code *Can. J. Phys.* **86** 675

[34] Stenke M., Aichele K., Harthiramani D., Hofmann G., Steidl M., Volpel R. and Salzborn E. 1995 Electron-impact single-ionization of singly and multiply charged tungsten ions *J. Phys. B: At. Mol. Opt. Phys.* **328** 2711

[35] Spruck K., Becker A. Borovik A., Gharaibeh M.F., Rausch J., Schippers S. and Müller A. 2014 Electron-impact ionization of multiply charged tungsten ions *J. Phys.: Conf. Ser.* **488** 062026

[36] Mitnik D., Mandelbaum P., Schwob J.L., Bar-Shalom A. and Oreg J. 1997 Excitation-autoionization cross sections and rate coefficients of Zn-like ions *Phys. Rev. A* **55** 307

[37] Jonauskas V., Kynienė A., Kučas S. Pakalka S., Masys Š., Prancikevičius A. Borovik A., Gharaibeh M.F., Schippers S. and Müller A. 2019 Electron-impact ionization of W^{5+} *Phys. Rev. A* **100** 062701

[38] Zhang D., Xie L., Jiang J., Wu Z., Dong C., Shi Y. and Qu Y. 2018 Electron-impact single ionizaiton for W^{4+} and W^{5+} *Chin. Phys. B* **27** 053402